Pioneer. Adv. Mater. 2026. 1(1): 8-13 *DOI: 10.48308/piadm.2025.105735*

Shahid Beheshti University

Pioneering Advances in Materials

Journal homepage: http://piadm.sbu.ac.ir ISSN: XXXX

Research paper

Geometric Asymmetry and 2D Material Engineering in Plasmon-Induced Transparency Filters

Mohammad Amin Khanpour, Rouhollah Karimzadeh*

Department of Physics, Shahid Beheshti University, Tehran, Iran

* *r_karimzadeh@sbu.ac.ir*

Article info:

Article history:

Received: 07/02/2025

Accepted: 12/05/2025

Keywords: Plasmon-Induced Transparency (PIT), Asymmetric structures, Tunable filters, Micro photonic devices

Abstract

This study investigates the optimization of plasmon-induced transparency (PIT) structures incorporating two-dimensional materials for advanced optical filtering applications in the terahertz spectrum. Through systematic finite difference time domain simulations, we analyze how structural symmetry breaking, material composition variation, and electronic tuning affect filtering performance. Transitioning from symmetric to asymmetric configurations significantly enhances filtering efficiency by increasing transparency window count and improving absorption peak definition, with optimal results achieved in semi-asymmetric alignments. The introduction of additional graphene dark modes refines spectral characteristics through cross-coupling mechanisms, though with diminishing returns as mode count increases. Fermi energy tuning of graphene (0.4-1.0 eV) enables dynamic spectral control, producing predictable window shifts of approximately 0.8-1.0 THz per 0.2 eV increase, with higher values progressively flattening transparency windows above 40 THz. Substituting graphene with anisotropic phosphorene in selected dark modes introduces material-dependent spectral broadening, offering additional customization options at the expense of window sharpness. These findings reveal crucial design principles for high-performance, frequency-selective filters, highlighting the interplay between geometric configuration, material selection, and electronic tunability in PIT-based photonic devices.

1. Introduction

With the emergence of optical devices as a prominent component of modern technology, the demand for reliable and efficient optical filters has significantly increased[1], [2]. These filters are essential in a variety of applications, including optical communication systems[3], [4], sensing[5], [6], and integrated photonic circuits[7]. An ideal optical filter should possess a dynamic operational range, be compact, and exhibit a high degree of absorption for unwanted wavelengths while allowing the desired frequency to pass through with an ultra-narrow

bandwidth. Meeting these stringent requirements has driven the exploration of advanced filtering techniques[8], [9], [10], [11], [12]. One method that has been widely studied is Electromagnetically Induced Transparency (EIT), a quantum interference phenomenon that enables narrowband filtering and slow-light effects. While EIT-based filters offer promising performance, their practical implementation faces challenges, including high manufacturing costs, complex experimental setups, and sensitivity to noise and environmental fluctuations. These limitations have motivated researchers to explore alternative approaches, leading to the development of Plasmon-Induced Transparency as a competing and more practical process[13], [14], [15], [16], [17], [18], [19].

PIT is a classical analog of EIT and is achieved through the destructive interference between resonant modes in plasmonic structures. These modes are typically categorized into two types: bright modes, which strongly couple to the external electromagnetic field, and dark modes, which weakly interact with the field but strongly couple to the bright modes. By carefully designing the interaction between these modes, PIT structures can exhibit a transparency window within an otherwise opaque spectrum due to destructive interference of the plasmonic wave of each mode. This phenomenon allows PIT-based filters to achieve the desired combination of narrowband transmission and high selectivity while benefiting from the scalability and compactness of plasmonic systems[20], [21], [22].

In recent years, significant attention has been directed toward enhancing the performance of PIT structures using innovative design approaches. One such approach involves the incorporation of two-dimensional (2D) materials into PIT structures in place of metallic components that are usually used for such structures[23]. Materials like graphene, transition metal dichalcogenides (TMDs), and hexagonal boron nitride have been extensively employed due to properties such as low loss, compactness, and ability to form surface plasmons. These 2D materials not only improve the performance of PIT structures by their lower loss rate but also contribute to the miniaturization of the overall device. This makes them particularly attractive for integration into compact photonic systems[24].

Another area of interest in enhancing PIT structures is the incorporation of multiple dark modes. Introducing multiple dark modes can significantly alter the absorption profile of the system, providing additional degrees of freedom for tailoring the transparency window[25], [26], [27]. By carefully selecting and configuring these dark modes, researchers can design filters with specific transmission characteristics, thereby broadening the applicability of PIT-based devices in optical communications and sensing[28], [29].

A relatively unexplored aspect is the effect of asymmetric placement of dark modes within the structure. Asymmetry in the arrangement of dark modes introduces novel interference effects, potentially modifying the spectral profile of the filter in unique ways[13], [30], [31]. Understanding these effects could provide valuable insights into optimizing PIT structures for specific applications, enabling the development of more efficient and versatile optical filters.

Moreover, there is growing interest in utilizing different materials as dark modes within the same structure. Employing multiple materials allows for a more diverse range of optical responses, which could lead to enhanced filtering capabilities, improved tunability, and greater flexibility in device design. Exploring how these materials interact within the PIT framework and how their unique properties contribute to the overall performance remains an exciting and active area of research[32], [33], [34], [35].

The present work begins with evaluating the performance of a PIT structure incorporating one, two, and three layers of dark modes of the same material type, using graphene for all dark modes. This initial setup provides a baseline for understanding the behavior of asymmetric dark mode arrangements PIT filters under more controlled, homogeneous conditions. The spatial distribution of these modes plays a key role in determining the filter's spectral profile. Here we seek to find out the exact effect of the introduction of asymmetry into the system. The study then progresses to investigate how the performance changes when the dark modes are fabricated from different materials, assessing the impact of material diversity on the overall behavior of the PIT structure. This approach offers insights into the role of material

composition in optimizing the filtering characteristics, such as bandwidth, transparency depth, and tunability. Furthermore, as the work progresses, the influence of adjusting the Fermi energy of graphene in these mixed-material structures will be explored. This analysis will provide deeper insights into how changing the Fermi energy can fine-tune the performance of the PIT structure, specifically within different regions of the electromagnetic spectrum.

2. Geometrical Design and Refraction Index of Dark Mode Materials

To investigate the interactions among asymmetric dark modes and their effect on the filtering performance of the PIT structure, a multi-layer structure was selected as the template for this study, as shown in Figure 1. The design features two phosphorene ribbons, each 120 nm wide and separated by 200 nm along the x-axis, which act as the bright mode. The structure possesses a substrate with a constant refractive index of 1.6. The dark modes are implemented as ribbons with a uniform thickness of 1 nm. The structure incorporates three layers of dark modes, each having a consistent width of 320 nm. Importantly, the spacing between the dark modes along the y-axis is non-uniform, varying based on achieving optimal filtering performance. At the bottom of the structure, a 50 nm gold layer is embedded to serve as a wave reflector.

The numerical simulations in this study were performed using the finite difference time domain simulations. The electromagnetic wave interactions were modeled by solving Maxwell's equations with appropriate boundary conditions. Periodic boundary conditions were applied in the x-direction to simulate an infinitely extended structure, while perfectly matched layers (PML) were implemented in the y-direction to prevent reflections. The structure was excited using a plane wave with normal incidence, and the absorption spectra were calculated by evaluating the ratio of absorbed power to incident power. This comprehensive simulation approach allowed for accurate evaluation of the electromagnetic response across the frequency range of 25-60 THz, capturing all relevant plasmon-induced transparency phenomena with high fidelity.

A key characteristic of this design is the asymmetric placement of dark modes, which offers several unique advantages. Unlike conventional symmetric designs, where each dark mode typically interacts with only one underlying mode, the asymmetry in this structure facilitates interactions with multiple elements simultaneously. This expanded interaction capability allows each dark mode to couple with more than one underlying dark mode, leading to the formation of multiple Fabry-Perot cavities. As a result, additional absorption peaks emerge, enhancing the structure's spectral performance.

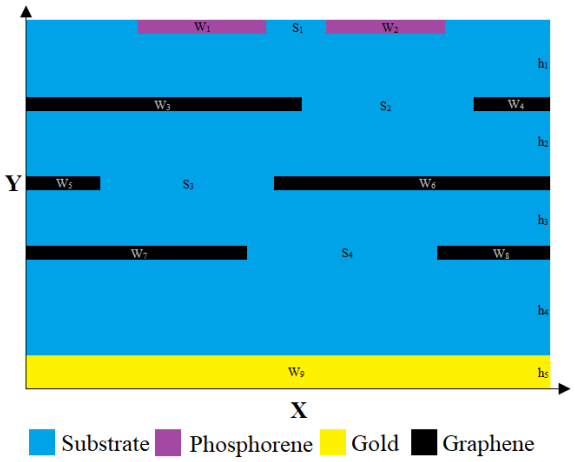

Figure 1. Schematic illustration of the multi-layer structure. The design features two bright mode ribbons, each 120 nm wide and with a separation of 60 nm between them (W_1=W_2=120 nm, S_1=60 nm), positioned on a substrate with a refractive index of 1.6. Dark modes, each 320 nm wide (W_3+W_4=W_5+W_6=W_7+W_8=320 nm), are placed asymmetrically with x direction separation of 180 nm (S_2=S_3=S_4=180 nm), creating variable distances between layers along the y-axis. A gold layer at the base acts as a wave reflector with a width of 500 nm and thickness of 50 nm (W_5=500 nm, h5=50 nm). In this configuration, Phosphorene is exclusively used for the bright modes, while the dark modes can be composed of either Graphene or Phosphorene. The total height of the structure is 1440 nm. (h_1+h_2+h_3+h_4+h_5=1440 nm)

Phosphorene and graphene were selected as bright and dark modes respectively for their exceptional material properties, making them particularly well-suited for integration into PIT

structures. Phosphorene exhibits significant anisotropy, a tunable bandgap ranging from 0.3 to 2 eV, and strong light-matter interactions across a wide spectral range, including the visible and infrared regions. These features make phosphorene highly effective in supporting surface plasmon resonances necessary for bright modes. Furthermore, phosphorene's bandgap tunability, which can be controlled through structural engineering or external fields, offers substantial flexibility in adjusting the spectral position and width of the PIT transparency window. In the latter part of this paper, phosphorene is used as one of the dark mode layers to see the effect it might have on the overall performance of the structure.

Graphene, on the other hand, is exclusively employed as a material for dark modes in this study, owing to its outstanding electrical conductivity, ultrafast carrier mobility, and low optical losses in the infrared and terahertz frequency ranges. The tunability of graphene's Fermi energy, which can be modulated through external gating or chemical doping, further enhances its adaptability, enabling precise control over the spectral position and width of the PIT window. This dynamic tunability is particularly valuable for applications that require real-time spectral reconfiguration, such as adaptive sensing and filtering technologies, providing the versatility needed for a wide range of advanced photonic systems. To use Phosphorene and Graphene, the permittivity of the 2d layer of these materials needs to be acquired.

For graphene, the surface conductivity, denoted as σ_g, can be expressed using the Drude model[36], [37]:

$$\sigma_g = \frac{ie^2 E_f}{\pi\hbar^2\left(\omega + i\tau^{-1}\right)} = \frac{ie^2}{\pi\hbar^2\left(\omega + i\tau^{-1}\right)} \left(\mathrm{sgn}(n)\hbar v_f \sqrt{\pi\left|\frac{\varepsilon_0\varepsilon_r}{te}\left(V + V_0\right)\right|}\right)$$

In this model, ω represents the angular frequency, while the electron-phonon relaxation time, τ, is given by $\tau = \mu E_f / e V_f^2$ where $v_F = 10^6\ ms^{-1}$ is the Fermi velocity, and $\mu = 1\times10^4\ cm^2v^{-1}s^{-1}$ represents the carrier mobility[38]. E_f denotes the Fermi energy of graphene, which is set to 0.6 eV in this study and the equation to calculate E_f based on externally applied voltage is also given in the above equation[39], where t represents the thickness of the graphene layer, n is the doping concentration, and the sign function accounts for whether the graphene is electron-doped ($n>0$) or hole-doped ($n<0$). V_0 denotes the voltage offset caused by natural doping in graphene, which is assumed to be zero in this work[39]. Based on this, the permittivity of graphene is derived as:

$$\varepsilon_g = \varepsilon_r + i\frac{\sigma_g}{\varepsilon_0\omega d_g}$$

Here, ε_0 is the vacuum dielectric constant. For monolayer graphene, the relative permittivity is known to be $\varepsilon_r = 2.5$, and the thickness of the graphene layer is $d_g = 0.34\ nm$[40].

The permittivity of a phosphorene layer can be represented as a diagonal matrix [41]:

$$\varepsilon = \begin{bmatrix} \varepsilon_{xx} & 0 & 0 \\ 0 & \varepsilon_{yy} & 0 \\ 0 & 0 & \varepsilon_{zz} \end{bmatrix}$$

Here, ε_{xx}, ε_{yy}, and ε_{zz} correspond to the permittivity components in the X, Y, and Z directions, respectively, and can be expressed as:

$$\varepsilon_{ii} = \varepsilon_r + \frac{i\sigma_{ii}}{\varepsilon_0\omega d}\left(i = x, \mathrm{y}, \mathrm{z}\right)$$

In this equation, ϵ_r is the relative permittivity, which is equal to 5.76 for phosphorene [42]. ε_0 is the permittivity of free space, d represents the thickness of the phosphorene layer, ω is the frequency of the incident light, σ_{ii} is the surface conductivity, and $\varepsilon_{zz} \cong 0$. According to the classical Drude model, the conductivity σ_{ii} of phosphorene is given by [34]:

$$\sigma_{ii} = \frac{iD_{ii}}{\pi\left(\omega + i\eta/\hbar\right)}\left(i = x, y\right)$$

Here, $\hbar$ is the reduced Planck's constant, and η represents the carrier momentum relaxation, which is considered to be 10 meV in this work[43][44]. The Drude weight, D_{ii}, is defined as:

$$D_{xx} = \frac{\pi e^2 n_s}{\left(\frac{\hbar^2}{2\gamma^2/\Delta + \eta_c}\right)}, D_{yy} = \frac{\pi e^2 n_s}{\left(\frac{\hbar^2}{\nu_c}\right)}$$

In this expression, e denotes the electron charge, n_s is the carrier density (assumed to be 10^{14} cm^{-2} [45], [46]). For phosphorene with a lattice constant a=0.223nm and a bandgap Δ = 2 eV[47], [48], the parameter values in the above equation are $\gamma = 4a/\pi$ eVm, $\eta_c = \hbar^2/(0.4m_0)$, and $\nu_c = \hbar^2/(0.7m_0)$[49]. Here, the rest mass of the electron is $m_0 = 9.10938 \times 10^{-31}$ kg[49], [50].
Figure 2 illustrates the variation in the real and imaginary components of the permittivity of graphene and phosphorene over a frequency range of 25 to 60 THz.

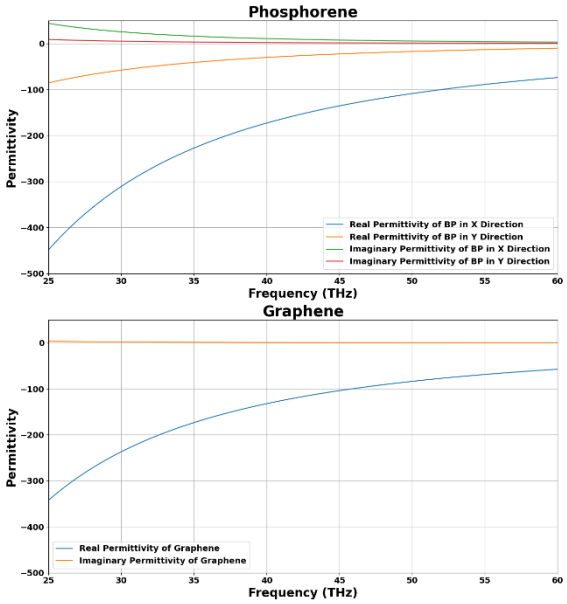

Figure 2. Plot showing the real and imaginary components of the permittivity for phosphorene along the X and Y directions and Graphene. The graph illustrates the anisotropic behavior of these materials, highlighting the differences in their dielectric properties in response to external electromagnetic fields.

3. Simulation Results

To initiate the analysis, the first graphene dark mode is positioned symmetrically at Y_1=50.5 nm from the bright mode (Figure 3(a)). This configuration represents a symmetric alignment. Subsequently, the dark mode is incrementally shifted along the x-axis, progressively introducing asymmetry until the positioning becomes fully asymmetric (Figure 3(c)). As illustrated in the graphs, the symmetric alignment primarily exhibits two transparency windows. However, in one of these windows (30–35 THz), one absorption peak demonstrates inefficiency, failing to effectively filter out the incident wave. In contrast, the fully asymmetric configuration results in three transparency windows, with all absorption peaks achieving an efficiency exceeding 80%. This performance is significantly superior to the symmetric arrangement.
Additionally, as the structure transitions from symmetric to fully asymmetric positioning, several intermediate absorption peaks of varying strengths emerge, as shown in Figure 3(d). Some of these intermediate configurations, such as the one depicted in Figure 3(b), offer more stable and desirable performance compared to both fully symmetric and fully asymmetric alignments. Considering these findings, the optimal filtering performance is achieved when the dark mode is positioned asymmetrically with a separation of 300 nm on one side and 20 nm on the other. This configuration delivers superior filtering efficiency within the frequency range of 25–45 THz.

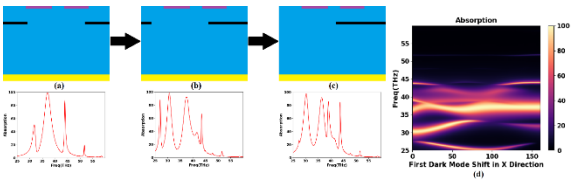

Figure 3. Variation in the absorption profile of the structure as it transitions from fully symmetric alignment (a) to fully asymmetric alignment (c). A comprehensive spectral profile is presented in (d), where a value of 160 represents the fully symmetric configuration, and 0 corresponds to the fully asymmetric configuration.

In the next step, the second dark mode is positioned at Y_2=77.5 nm. This dark mode is divided within the simulation cell, with 20 nm on the left side and 300 nm on the right side, creating a configuration that is neither fully symmetric nor fully asymmetric. Subsequently,

an additional graphene dark mode is introduced into the structure and incrementally shifted along the x-axis, transitioning from symmetric to asymmetric alignment. As shown in Figure 4, the symmetric alignment (Figure 4(a)) generates noticeably fewer and weaker transparency windows compared to the semi-asymmetric and fully asymmetric configurations. Moreover, one of the transparency windows formed in the fully asymmetric alignment exhibits a significantly higher degree of loss compared to the semi-asymmetric alignment, which negatively impacts its filtering performance. Additionally, a comparison of the results in Figure 3(b) and Figure 4(b) reveals that the transparency windows in the latter case are more closely spaced, with a reduction in transparency efficiency. For instance, at a frequency of 29 THz, the degree of loss increases from 15% in the semi-asymmetric alignment (Figure 3(b)) to 22.5% in the configuration shown in Figure 4(b). This indicates that while the introduction of additional dark modes can enhance spectral characteristics in certain cases, careful alignment is critical to optimize filtering performance.

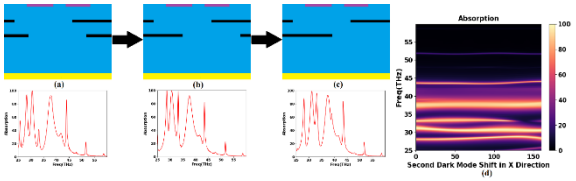

Figure 4. Variation in the absorption profile of the structure with two dark modes, where the first is set in a semi-asymmetric configuration. The structure transitions from fully symmetric alignment (a) to fully asymmetric alignment (c). A detailed spectral profile is shown in (d), with 160 representing the fully symmetric configuration and 0 denoting the fully asymmetric configuration.

Finally, the third and final graphene dark mode is introduced into the structure. The vertical separation between the second and third dark modes is set to Y_3=29 nm, while the horizontal position of the second dark mode is adjusted to have 208.5 nm on the left side and 111.5 nm on the right side of the structure. As illustrated in Figure 5, the addition of the third dark mode leads to an increase in the number of transparency windows, accompanied by a reduction in the width of both the absorption peaks and transparency windows. However, the maximum transparency value decreases as the number of dark modes and absorption peaks increases, particularly in the semi-asymmetric configuration. The optimal result in terms of the number of transparency windows (Figure 5(b)) is achieved when the third dark mode is positioned with 17 nm on the left side and 303 nm on the right side. This configuration strikes a balance between maximizing transparency window count and maintaining desirable filtering performance.

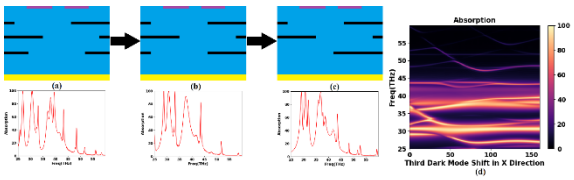

Figure 5. Variation in the absorption profile of the structure with three dark modes, where the first and second dark modes are set in semi-asymmetric configurations. The structure transitions from fully symmetric alignment (a) to fully asymmetric alignment (c). A comprehensive spectral profile is presented in (d), with 160 representing the fully symmetric configuration and 0 corresponding to the fully asymmetric configuration.

The observed behavior in this structure can be attributed to several factors. One of the primary reasons is the cross-coupling between the dark modes. By introducing asymmetry into the arrangement of the dark modes, the structure enables not only direct coupling between adjacent dark modes but also weaker interactions with more distant dark modes and even the bright mode. This extended coupling network modifies the destructive interference patterns, resulting in significant changes to the absorption and transparency characteristics. Additionally, the staggered design of the structure creates multiple Fabry-Pérot cavities within the system. These cavities facilitate the excitation of specific frequencies while simultaneously introducing higher degrees of loss for other frequencies. This interplay between the staggered configuration and the Fabry-Pérot resonances contributes to the complex spectral behavior observed, enhancing the structure's ability to filter and

manipulate electromagnetic waves across a broader range of frequencies.

Now focusing on fully graphene-based structures, it is well established from Equation (1) that the surface conductivity of graphene is directly proportional to its Fermi energy. Additionally, Equation (1) also demonstrates that the Fermi Energy of graphene can be tuned by applying an external voltage. Building on this foundation, we investigate the effects of varying the Fermi energy of the three graphene dark modes. Previously, the Fermi energy of graphene was set at a constant value of 0.6 eV. For this study, we systematically adjust the Fermi energy to 0.4 eV, 0.6 eV, 0.8 eV, and 1.0 eV, as illustrated in Figures 6(a), 6(b), 6(c), and 6(d), respectively. The results reveal a clear trend: as the Fermi energy increases, both the absorption peaks and the transparency windows exhibit a spectral shift from lower to higher frequencies. Moreover, the primary absorption peak, located at 37.5 THz and originating from the phosphorene bright mode, remains fixed. However, the interaction between this bright mode absorption peak and the transparency windows, which are influenced by the graphene dark modes, leads to notable changes in the width and intensity of the main absorption peak. These findings highlight the dynamic interplay between the bright and dark modes and emphasize the potential of Fermi energy tuning to fine-tune the spectral characteristics of the PIT structure.

As shown in Figure 6(a), for a Fermi energy of 0.4 eV, the main absorption peak remains largely unaffected and is separated from the transparency window region. A minor interaction is observed near 38 THz, as indicated by a small transparency window, but overall, the main absorption peak remains intact and well-defined. In Figure 6(b), corresponding to a Fermi energy of 0.6 eV, the transparency windows have shifted closer to the main absorption peak. This overlap results in a reduction in both the width and intensity of the absorption peak. The diminished performance is attributed to the alignment of one transparency window with the frequency of the main absorption peak, causing interference. Additionally, it is observed that as the absorption peaks shift beyond the 40 THz region, their performance degrades. This suggests that the structure becomes less effective at confining electromagnetic waves at higher frequencies compared to lower ones. For a Fermi energy of 0.8 eV, shown in Figure 6(c), the superposition of another absorption peak on the main peak allows it to remain fully intact. However, the neighboring transparency windows further narrow the main peak's width while also reducing their transmission efficiency. Finally, when the Fermi energy is increased to 1.0 eV, as depicted in Figure 6(d), both the absorption peaks and the transparency windows exhibit weakened performance. This degradation indicates that the structure's ability to sustain strong resonance and effective filtering diminishes at higher Fermi energy levels. These results also indicate a trend toward window flattening at higher Fermi energies (e.g., 0.8–1.0 eV), where adjacent transparency windows begin to spectrally merge due to their shifted positions. This leads to a broader, less sharply defined transparency region, particularly in the 40–45 THz range, which can be advantageous in applications requiring wideband filtering or stable transmission. Thus, by tuning the Fermi level, the PIT structure can be dynamically engineered to exhibit either sharp, narrowband filtering or flatter, broadband characteristics, depending on the application.

To better illustrate the trends in PIT behavior with varying Fermi energy levels, a comparative analysis of the absorption spectra in Figures 6(a)–6(d) is essential. As the Fermi energy increases from 0.4 eV to 1.0 eV, the transparency windows exhibit a clear spectral shift toward higher frequencies, with an average displacement of approximately 0.8–1.0 THz per 0.2 eV increment. Moreover, the number and shape of the transparency windows evolve significantly. At lower Fermi levels (0.4–0.6 eV), the windows remain distinct and relatively narrow, while at higher levels (0.8–1.0 eV), adjacent windows begin to overlap, leading to the formation of broader, flatter transparency regions. This spectral merging reduces the sharpness of individual peaks but creates a more extended transmission band, particularly around the 40–45 THz range. This flattening effect becomes most prominent at 1.0 eV, where the PIT windows appear less isolated and more continuous. Such behavior is highly beneficial for broadband filtering and slow-light applications, where a flatter and more stable transmission profile is desired. Overall, the results confirm that Fermi energy tuning

provides a robust and dynamic mechanism for engineering the spectral characteristics of PIT structures.

The potential to achieve a broader or more flattened PIT window in our proposed structure is primarily governed by two key mechanisms: geometric asymmetry and Fermi energy tuning of the 2D materials. As shown in Figures 3 through 6, introducing asymmetric placement of dark modes increases the number of Fabry-Pérot-like resonant cavities and enables more complex interference patterns. These effects lead to the formation of multiple closely spaced transparency windows that, under optimized configurations, can begin to merge into a broader composite window. Additionally, tuning the Fermi energy of the graphene layers directly modulates the plasmonic resonance frequencies of the dark modes. At higher Fermi energies (e.g., 0.8 eV to 1.0 eV), the spectral response shifts in a manner that stretches and partially overlaps adjacent transparency features. While this sometimes reduces peak sharpness, it also results in a flatter, more extended transparency region, especially in the 40–45 THz range. These findings suggest that by strategically combining geometric asymmetry and Fermi level control, the structure can be engineered to support broader or flattened PIT windows, which are advantageous for applications requiring stable transmission over a wider spectral band, such as broadband filtering or slow light systems.

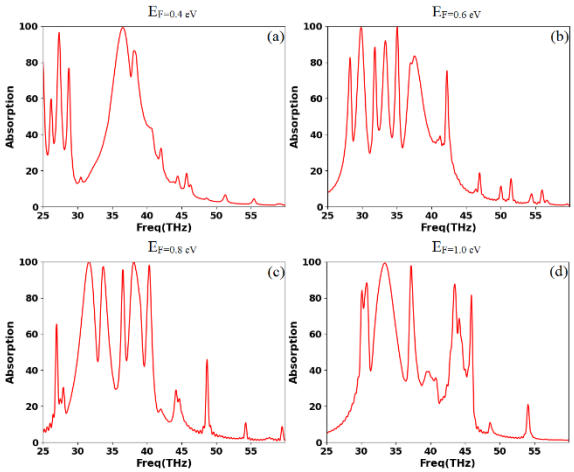

Figure 6. Absorption performance graphs of the graphene-based structure at varying Fermi energy levels: (a) 0.4 eV, (b) 0.6 eV, (c) 0.8 eV, and (d) 1.0 eV.

Another aspect of interest is the impact of substituting graphene with another 2D material, such as phosphorene, in the structure while keeping all other parameters unchanged. To investigate this, the material of one dark mode in the structure is replaced with phosphorene to evaluate its effect on the absorption and transparency performance of the system. The results are presented in Figure 7, showcasing the absorption profiles for the following configurations: (a) all dark modes composed of graphene, (b) the first dark mode replaced with phosphorene, (c) the second dark mode replaced with phosphorene, and (d) the third dark mode replaced with phosphorene. From the results, it can be observed that introducing phosphorene primarily leads to a broadening of the existing absorption peaks. This broadening reduces the clarity of some transparency windows, as they become partially or fully covered by the expanded absorption regions. The degree of this effect varies depending on which dark mode is replaced with phosphorene. For instance, in Figure 7(d), the substitution of phosphorene in the third dark mode results in a noticeable broadening that adversely affects the performance of a transparency window. These findings highlight that while the use of phosphorene can introduce distinct changes to the absorption profile, it may also compromise the filtering performance by reducing the transparency window sharpness and coverage.

The strategic incorporation of phosphorene as a dark mode material represents a deliberate approach to modulate the spectral response of the PIT structure through material diversity. Unlike graphene, which exhibits isotropic electronic properties, phosphorene's inherently anisotropic nature introduces direction-dependent plasmonic behavior. This anisotropy manifests as broader absorption peaks when phosphorene replaces graphene in the dark modes, as evidenced in Figure 7(b-d). The broadening effect stems from phosphorene's unique band structure and lower electron mobility compared to graphene, resulting in increased damping of plasmonic oscillations. Specifically, when phosphorene is used as a dark mode material, it alters the coupling dynamics between bright and dark modes, modifying both the strength and spectral range of the destructive interference responsible for transparency windows. This material-induced spectral

engineering provides an additional degree of freedom beyond geometric manipulation and Fermi energy tuning, albeit at the cost of reduced transparency window sharpness. These findings illuminate the fundamental trade-offs between peak broadening and transparency efficiency when incorporating anisotropic 2D materials into PIT structures, offering valuable insights for material selection in application-specific filter design.

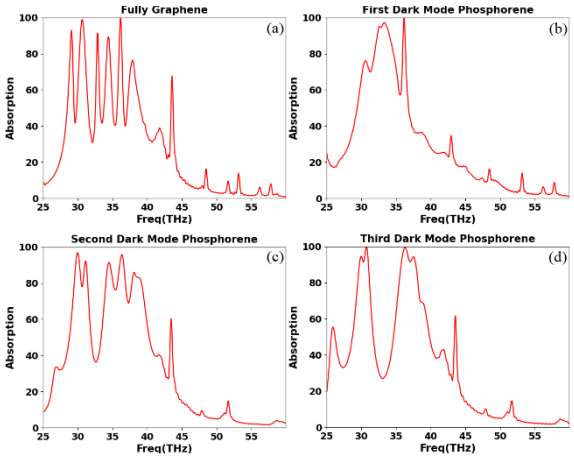

Figure 7. Absorption profiles of the structure under different material configurations: (a) all dark modes composed of graphene, (b) the first dark mode replaced with phosphorene, (c) the second dark mode replaced with phosphorene, and (d) the third dark mode replaced with phosphorene.

These findings highlight that while the use of phosphorene can introduce distinct changes to the absorption profile, it may also compromise the filtering performance by reducing the transparency window sharpness and coverage.

4. Conclusion

This study systematically explored the influence of structural symmetry, material composition, and Fermi energy tuning on the absorption and transparency performance of plasmon-induced transparency (PIT) structures incorporating graphene and phosphorene dark modes. The results demonstrated that transitioning from symmetric to asymmetric configurations significantly enhances the filtering performance by increasing the number of transparency windows and improving absorption peak efficiency. Specifically, the optimal performance was achieved with a semi-asymmetric alignment, where the separation between the dark modes was carefully adjusted to balance peak width and transmission power. This highlights the critical role of geometric asymmetry in optimizing PIT structures. The introduction of additional graphene dark modes further refined the spectral characteristics but revealed a trade-off between the number of transparency windows and their overall efficiency. In particular, the addition of a third dark mode increased the number of transparency windows while reducing their sharpness and transmission power, emphasizing the need for precise mode placement to maintain performance. Tuning the Fermi energy of graphene emerged as another pivotal factor in controlling the spectral behavior. Adjusting the Fermi energy from 0.4 eV to 1.0 eV resulted in spectral shifts of the absorption peaks and transparency windows, with higher Fermi energies leading to diminished performance at higher frequencies. This underlines the potential of external voltage control as a mechanism for dynamically optimizing PIT structures for specific frequency ranges. Finally, the substitution of graphene with phosphorene in one of the dark modes revealed the material's potential to broaden absorption peaks, thereby altering the transparency window profile. While this material substitution introduced notable spectral changes, it also reduced the sharpness and efficiency of transparency windows, underscoring the need for careful material selection to achieve desired filtering characteristics. In conclusion, this work provides valuable insights into the intricate interplay between geometry, material composition, and electronic tunability in PIT structures. These findings pave the way for the design of advanced tunable filters and sensors that leverage the unique properties of 2D materials to achieve high-performance, frequency-specific functionality across the terahertz spectrum.

References

1. *L. Shen, L. Lu, Z. Guo, L. Zhou, and J. Chen, "Silicon optical filters reconfigured from a 16 × 16 Benes switch matrix," Opt. Express, vol. 27,*

no. 12, p. 16945, 2019, doi: 10.1364/oe.27.016945.

2. *J. P. Biethan, D. Arhilger, J. Pistner, H. Reus, M. Stapp, and H. Hagedorn, "High precision optical filter based on magnetron sputtering: Direct coating on glass and silicon wafers," Vak. Forsch. und Prax., vol. 29, no. 4, pp. 26–31, 2017, doi: 10.1002/vipr.201700654.*
3. *T. A. Huffman, G. M. Brodnik, C. Pinho, S. Gundavarapu, D. Baney, and D. J. Blumenthal, "Integrated resonators in an ultralow loss Si3N4/SiO2 platform for multifunction applications," IEEE J. Sel. Top. Quantum Electron., vol. 24, no. 4, 2018, doi: 10.1109/JSTQE.2018.2818459.*
4. *L. R. Chen, J. Wang, B. Naghdi, and I. Glesk, "Subwavelength grating waveguide devices for telecommunications applications," IEEE J. Sel. Top. Quantum Electron., vol. 25, no. 3, 2019, doi: 10.1109/JSTQE.2018.2879015.*
5. *D. Liu, H. Xu, Y. Tan, Y. Shi, and D. Dai, "Silicon photonic filters," 2021. doi: 10.1002/mop.32509.*
6. *K. Abdelsalam et al., "Tunable dual-channel ultra-narrowband Bragg grating filter on thin-film lithium niobate," Opt. Lett., vol. 46, no. 11, p. 2730, 2021, doi: 10.1364/ol.427101.*
7. *S. Robinson, "Photonic crystal ring resonator based optical filters for photonic integrated circuits," 2014, pp. 131–138. doi: 10.1063/1.4898231.*
8. *R. Rajasekar, "Numerical Investigation of Nanoresonator Based Ultra Narrow-Band Photonic Filters," IEEE Trans. Nanotechnol., vol. 23, pp. 188–194, 2024, doi: 10.1109/TNANO.2024.3370717.*
9. *O. Aharon and I. Abdulhalim, "Tunable optical filter having a large dynamic range," Opt. Lett., vol. 34, no. 14, p. 2114, 2009, doi: 10.1364/ol.34.002114.*
10. *B. Ni et al., "Design of Dual Narrow-Band Optical Filter Based on Plasmonic Split-Ring Dimer Metasurface," IEEE Photonics Technol. Lett., vol. 36, no. 15, pp. 969–972, 2024, doi: 10.1109/LPT.2024.3419223.*
11. *M. Amin Khanpour, F. Moradiani, G. M. Parsanasab, and R. Karimzadeh, "An investigation on the effects of geometrical parameters on the sensitivity of micro-disk and micro-ring plasmonic sensors," Opt. Laser Technol., vol. 162, no. January, p. 109236, Jul. 2023, doi: 10.1016/j.optlastec.2023.109236.*
12. *M. Alijabbari, R. Karimzadeh, S. Pakniyat, and J. S. Gomez-Diaz, "Dual-band and spectrally selective infrared absorbers based on hybrid gold-graphene metasurfaces," Opt. Express, vol. 32, no. 9, p. 16578, Apr. 2024, doi: 10.1364/oe.522046.*
13. *Z.-G. Dong et al., "Role of asymmetric environment on the dark mode excitation in metamaterial analogue of electromagnetically-induced transparency," Opt. Express, vol. 18, no. 21, p. 22412, Oct. 2010, doi: 10.1364/oe.18.022412.*
14. *Y. Liu et al., "Plasmon-induced transparency in a reconfigurable composite valley photonic crystal," Opt. Express, vol. 30, no. 3, p. 4381, 2022, doi: 10.1364/oe.447946.*
15. *K. Sun et al., "Graphene-enhanced hybrid terahertz metasurface sensor for ultrasensitive nortriptyline sensing and detection," Opt. Express, vol. 30, no. 20, p. 35749, 2022, doi: 10.1364/oe.470772.*
16. *M. Mao et al., "Realizing PIT-like transparency via the coupling of plasmonic dipole and ENZ modes," Opt. Express, vol. 30, no. 6, p. 8474, 2022, doi: 10.1364/oe.450423.*
17. *Z. Ling, Y. Zeng, G. Liu, L. Wang, and Q. Lin, "Unified model for plasmon-induced transparency with direct and indirect coupling in borophene-integrated metamaterials," Opt. Express, vol. 30, no. 12, p. 21966, 2022, doi: 10.1364/oe.462815.*
18. *B. Tang, Z. Guo, and G. Jin, "Polarization-controlled and symmetry-dependent multiple plasmon-induced*

transparency in graphene-based metasurfaces," Opt. Express, vol. 30, no. 20, p. 35554, Sep. 2022, doi: 10.1364/oe.473668.

19. *P. Weis, J. L. Garcia-Pomar, R. Beigang, and M. Rahm, "Hybridization Induced Transparency in composites of metamaterials and atomic media," Opt. Express, vol. 19, no. 23, p. 23573, 2011, doi: 10.1364/oe.19.023573.*
20. *Z. Ye et al., "Mapping the near-field dynamics in plasmon-induced transparency," Phys. Rev. B - Condens. Matter Mater. Phys., vol. 86, no. 15, 2012, doi: 10.1103/PhysRevB.86.155148.*
21. *G. Cao, H. Li, Y. Deng, S. Zhan, Z. He, and B. Li, "Plasmon-induced transparency in a single multimode stub resonator," Opt. Express, vol. 22, no. 21, p. 25215, 2014, doi: 10.1364/oe.22.025215.*
22. *P. C. Wu et al., "Magnetic plasmon induced transparency in three-dimensional metamolecules," Nanophotonics, vol. 1, no. 2, pp. 131–138, 2012, doi: 10.1515/nanoph-2012-0019.*
23. *C. Xiong et al., "Dynamically controllable multi-switch and slow light based on a pyramid-shaped monolayer graphene metamaterial," Phys. Chem. Chem. Phys., vol. 23, no. 6, pp. 3949–3962, 2021, doi: 10.1039/d0cp06182d.*
24. *Z. Cai, Y. Xu, C. Wang, and Y. Liu, "Polariton Photonics Using Structured Metals and 2D Materials," 2020. doi: 10.1002/adom.201901090.*
25. *M. A. Khanpour and R. Karimzadeh, "Transparency window in the THz frequency based on asymmetric dark-dark modes interaction," Opt. Mater. Express, vol. 13, no. 7, p. 1895, Jul. 2023, doi: 10.1364/ome.493402.*
26. *Z. Liu et al., "Simultaneous switching at multiple frequencies and triple plasmon-induced transparency in multilayer patterned graphene-based terahertz metamaterial," New J. Phys., vol. 22, no. 8, 2020, doi: 10.1088/1367-2630/ab9e8a.*
27. *B. Wang, X. Wang, X. Yan, C. Yu, and T. Wang, "Dynamically Tunable Terahertz Multiple Plasmon-Induced Transparency and Slow Light in Planar Metamaterials With Rectangular Interrupted Graphene," Int. J. Quantum Chem., vol. 124, no. 24, p. e27526, 2024, doi: 10.1002/qua.27526.*
28. *J. Zhang, J. Li, S. Chen, K. Wen, and W. Liu, "Quadruple Plasmon-Induced Transparency and Dynamic Tuning Based on Bilayer Graphene Terahertz Metamaterial," Nanomaterials, vol. 13, no. 17, p. 2474, Sep. 2023, doi: 10.3390/nano13172474.*
29. *Y. Zhang et al., "Plasmon-induced transparency effect in hybrid terahertz metamaterials with active control and multi-dark modes," Chinese Phys. B, vol. 31, no. 6, p. 068702, 2022, doi: 10.1088/1674-1056/ac4f56.*
30. *X. Zhang et al., "Plasmonics: Asymmetric excitation of surface plasmons by dark mode coupling," Sci. Adv., vol. 2, no. 2, 2016, doi: 10.1126/sciadv.1501142.*
31. *X. Zheng, Z. Zhao, W. Shi, and W. Peng, "Broadband terahertz plasmon-induced transparency via asymmetric coupling inside meta-molecules," Opt. Mater. Express, vol. 7, no. 3, p. 1035, 2017, doi: 10.1364/ome.7.001035.*
32. *M. Li, Y. Shi, X. Liu, J. Song, X. Wang, and F. Yang, "Tunable plasmon-induced transparency in graphene-based plasmonic waveguide for terahertz band-stop filters," J. Opt. (United Kingdom), vol. 24, no. 6, 2022, doi: 10.1088/2040-8986/ac695f.*
33. *M. Z. Mashayekhi, K. Abbasian, and T. Nurmohammadi, "Dual-wavelength active and tunable modulation at telecommunication wavelengths using graphene-metal hybrid metamaterial based on plasmon induced transparency," Phys. Scr., vol. 97, no. 9, 2022, doi: 10.1088/1402-4896/ac86ad.*

34. *K. Wu et al., "Slow-light analysis based on tunable plasmon-induced transparency in patterned black phosphorus metamaterial," J. Opt. Soc. Am. A, vol. 38, no. 3, p. 412, 2021, doi: 10.1364/josaa.413384.*
35. *S. Xia, X. Zhai, L. Wang, and S. Wen, "Plasmonically induced transparency in in-plane isotropic and anisotropic 2D materials," Opt. Express, vol. 28, no. 6, p. 7980, 2020, doi: 10.1364/oe.389573.*
36. *Z. Zanbouri, Y. Hajati, and M. Sabaeian, "Investigation of anisotropic absorption in the hybrid L-shaped graphene-black phosphorene structure," Phys. E Low-Dimensional Syst. Nanostructures, vol. 146, no. October 2022, p. 115554, 2023, doi: 10.1016/j.physe.2022.115554.*
37. *M. Jablan, H. Buljan, and M. Soljačić, "Plasmonics in graphene at infrared frequencies," Phys. Rev. B - Condens. Matter Mater. Phys., vol. 80, no. 24, pp. 1–7, 2009, doi: 10.1103/PhysRevB.80.245435.*
38. *B. Tang, Z. Jia, L. Huang, J. Su, and C. Jiang, "Polarization-Controlled Dynamically Tunable Electromagnetically Induced Transparency-Like Effect Based on Graphene Metasurfaces," IEEE J. Sel. Top. Quantum Electron., vol. 27, no. 1, 2021, doi: 10.1109/JSTQE.2020.3021589.*
39. *J. Luan et al., "A Compact Graphene Modulator Based on Localized Surface Plasmon Resonance with a Chain of Metal Disks," Plasmonics, vol. 14, no. 6, pp. 1949–1954, Dec. 2019, doi: 10.1007/s11468-019-00995-w.*
40. *Y. L. Xu, H. X. Li, Y. Y. Wu, L. F. Li, Z. P. Zhang, and S. J. Qin, "Broadband electromagnetically induced transparency-like manipulation of graphene-black phosphorus hybrid metasurface," J. Phys. D. Appl. Phys., vol. 54, no. 44, 2021, doi: 10.1088/1361-6463/ac1a9f.*
41. *A. Nagarajan, K. van Erve, and G. Gerini, "Ultra-narrowband polarization insensitive transmission filter using a coupled dielectric-metal metasurface," Opt. Express, vol. 28, no. 1, p. 773, 2020, doi: 10.1364/oe.383781.*
42. *Y. M. Qing, H. F. Ma, and T. J. Cui, "Strong coupling between magnetic plasmons and surface plasmons in a black phosphorus-spacer-metallic grating hybrid system," Opt. Lett., vol. 43, no. 20, p. 4985, Oct. 2018, doi: 10.1364/ol.43.004985.*
43. *T. Low et al., "Plasmons and screening in monolayer and multilayer black phosphorus," Phys. Rev. Lett., vol. 113, no. 10, pp. 5–9, 2014, doi: 10.1103/PhysRevLett.113.106802.*
44. *J. Wang and Y. Jiang, "Infrared absorber based on sandwiched two-dimensional black phosphorus metamaterials," Opt. Express, vol. 25, no. 5, p. 5206, Mar. 2017, doi: 10.1364/oe.25.005206.*
45. *S. Ge et al., "Dynamical Evolution of Anisotropic Response in Black Phosphorus under Ultrafast Photoexcitation," Nano Lett., vol. 15, no. 7, pp. 4650–4656, Jul. 2015, doi: 10.1021/acs.nanolett.5b01409.*
46. *C. Liu et al., "Dynamically tunable excellent absorber based on plasmon-induced absorption in black phosphorus nanoribbon," J. Appl. Phys., vol. 127, no. 16, 2020, doi: 10.1063/5.0005449.*
47. *H. Zhang, B. Zeng, E. Gao, P. Yao, C. Liu, and H. Li, "Dynamically tunable terahertz sensors based on dual-layered graphene metamaterial," Opt. Commun., vol. 506, Mar. 2022, doi: 10.1016/j.optcom.2021.127555.*
48. *A. Chaves, W. Ji, J. Maassen, T. Dumitrică, and T. Low, "Theoretical overview of black phosphorus," 2D Mater. Prop. Devices, no. October, pp. 381–412, 2017, doi: 10.1017/9781316681619.022.*
49. *X. Cao and J. Guo, "Simulation of phosphorene field-effect transistor at the scaling limit," IEEE Trans. Electron Devices, vol. 62, no. 2, pp. 659–665, 2015, doi: 10.1109/TED.2014.2377632.*

50. J. Qiao, X. Kong, Z. X. Hu, F. Yang, and W. Ji, "High-mobility transport anisotropy and linear dichroism in few-layer black phosphorus," Nat. Commun., vol. 5, pp. 1–7, 2014, doi: 10.1038/ncomms5475.